



Hydromechanical state of soil fluidisation: a microscale perspective

Shay Haq¹ · Buddhima Indraratna² · Thanh T. Nguyen³ · Cholachat Rujikiatkamjorn¹

Received: 7 December 2021 / Accepted: 4 August 2022 / Published online: 31 October 2022
 © The Author(s) 2022

Abstract

This paper investigates soil fluidisation at the microscale using the discrete element method (DEM) in combination with the lattice Boltzmann method (LBM). Numerical simulations were carried out at varying hydraulic gradients across the granular assembly of soil. The development of local hydraulic gradients, the contact distribution, and the associated fabric changes were investigated. Microscale findings suggest that a critical hydromechanical state inducing fluid-like instability of a granular assembly can be defined by a substantial increase in grain slip associated with a rapid reduction in interparticle contacts. Based on these results, a new micromechanical criterion is proposed to characterise the transformation of granular soil from a hydromechanically stable to an unstable state. The constraint ratio (ratio of the number of constraints to the number of degrees of freedom) is introduced to portray the relative slippage between particles and the loss of interparticle contacts within the granular fabric. Its magnitude of unity corresponds to the condition of zero effective stress, representing the critical hydromechanical state. In practical terms, the results of this study reflect the phenomenon of subgrade mud pumping that occurs in railways when heavy-haul trains pass through at certain axle loads and speeds.

Keywords Constraint ratio · Critical hydraulic gradient · Discrete element method · Fluidisation · Lattice Boltzmann method

List of symbols

B Weighing function to correct the collision phase due to the presence of solid particles
 B_R Percentage of broken contacts
 c_L Lattice speed

c_n Viscoelastic damping constant for normal contact
 c_s Sound celerity
 c_t Viscoelastic damping constant for tangential contact
 d_p Diameter of the particle
 d_{50} Particle size that is 50% finer by mass in the particle size distribution
 d_{85} Particle size that is 85% finer by mass in the particle size distribution
 E^* Equivalent Young's modulus
 e_α^v Microscopic fluid velocity
 e_{oi}^k Initial void ratio of the k th layer
 e_{oi}^{avg} Initial void ratio of the entire sample considering all ten layers
 e_r Coefficient of restitution
 f_{bu} Static buoyancy force on the particle
 f_{hyd}^p Total hydrodynamic force (including the static buoyancy force) on the particle p
 f_f Hydrodynamic forces on the particle without buoyancy force
 f_g^p Gravitational force on the particle p
 f_j^c Force vector in j th direction at contact c
 f^T Tangential contact force

✉ Buddhima Indraratna
 Buddhima.Indraratna@uts.edu.au

Shay Haq
 Shay.Haq@student.uts.edu.au

Thanh T. Nguyen
 thanh.nguyen-4@uts.edu.au

Cholachat Rujikiatkamjorn
 Cholachat.Rujikiatkamjorn@uts.edu.au

¹ School of Civil and Environmental Engineering, Faculty of Engineering and IT, University of Technology Sydney (UTS), Sydney, NSW 2007, Australia

² Transport Research Centre, School of Civil and Environmental Engineering, Faculty of Engineering and IT, University of Technology Sydney (UTS), Sydney, NSW 2007, Australia

³ Transport Research Centre, School of Civil and Environmental Engineering, Faculty of Engineering and IT, University of Technology Sydney (UTS), Sydney, NSW 2007, Australia

f^N	Normal contact force	v_n^{rel}	Normal component of the relative velocity of two spherical particles
$f_\alpha(x, t)$	Particle distribution function	v_t^{rel}	Tangential component of the relative velocity of two spherical particles
$f_\alpha(x, t^*)$	Particle distribution function after the collision of fluid particles	v^p	Translational velocity of the particle p
$f_\alpha^{\text{eq}}(x, t)$	Equilibrium distribution function	w^p	Angular velocity of the particle p
G^*	Equivalent shear modulus	ω_α	Weighing factor for the microscopic fluid velocity
I^p	Moment of inertia of the particle p	x^n	Coordinate of the lattice cell
i_o	Overall applied hydraulic gradient	x_i^p	Centre of mass of the particle
$i_{o,\text{cr}}$	Critical overall hydraulic gradient of the soil specimen	z	Location of the particle
i_{hyd}	Local hydraulic gradient in a layer	Z	Coordination number
k_n	Elastic constant for normal contact	$Z_{\text{avg.}}$	Average coordination number
k_t	Elastic constant for tangential contact	ΔP	Pressure drop across the particle bed
L	Height of the particle bed	Δx	Lattice spacing
M	Mach number	ρ_f	Fluid density
M_s	Fraction of mechanically stable particles	δ_n	Normal overlap
m^p	Mass of the particle p	δ_t	Tangential overlap
m^*	Equivalent mass	Ω_α	Collision operator
N	Lattice resolution	$\Omega_\alpha^{\text{BGK}}$	Collision operator of the BGK model
N_c	Number of contacts	Ω_α^s	Additional collision term for solid fraction,
N_d	Number of degrees of freedom	ε_s	Solid fraction in the fluid cell volume
N_{ct}	Number of constraints	τ	Relaxation time
N_c^p	Number of contacts on particle p	μ_s	Coefficient of sliding friction
N_p	Number of particles	μ_f	Dynamic viscosity of the fluid
$N_p^{\geq 4}$	Number of particles with at least 4 or more contacts	σ'_{ij}	Cauchy effective stress tensor in the selected region
n	Overall porosity of the soil specimen	$\sigma'_{ij}{}^p$	Average stress tensor within a particle p
$n_i^{c,p}$	Unit-normal vector from the particle' centroid to the contact location	σ'_{zz}	Cauchy effective stresses of the particles in a layer in the fluid flow direction at any time
n_L	Number of layers	σ'_{zZo}	Initial Cauchy effective stresses of the particles in a layer in the fluid flow direction
O_i	Initial centroidal location of particle i		
O_j	Initial centroidal location of particle j		
O'_j	Displaced centroidal location of particle j		
R	Constraint ratio for a three-dimensional particle system with only sliding resistance		
R^*	Equivalent radius		
Re_p	Reynold's number of the particle		
S	Variance in the void ratios		
S_i	Slipping index		
S_c	Fraction of slipping contacts		
T_f^p	Fluid-particle interaction torque		
T_j^c	Interparticle contact torque due to tangential force		
t	Time		
t^*	Time after the collision		
u	Macroscopic fluid velocity		
u_{max}	Maximum velocity of the fluid flow in physical units		
V	Volume of the selected region or layer		
V^p	Volume of particle p		
v_d	Superficial or discharge velocity of the fluid		
v_f	Kinematic viscosity of fluid		

1 Introduction

A major problem leading to railroad instability that creates immense maintenance costs is related to the degradation of the soft subgrade and its potential for fluidisation or mud-pumping [7, 13, 24, 30, 40]. In this context, fluidisation is defined as when saturated soils are exposed to excessive hydraulic gradients and lose their intergranular contacts to transform into a fluid-like state. As a result, this slurry of fine particles migrates (pumps) into the overlying coarser ballast layer, hence the commonly used term mud-pumping, as investigated experimentally [2, 13, 27, 30]. These laboratory tests enable a better understanding of the hydromechanical behaviour of the subgrade soils, but primarily at the macroscale. From a micromechanical perspective, i.e. at the grain level, slippage and/or breakage of

the interparticle contacts and the resulting fabric evolution may initiate the transition from a hydromechanically stable to an unstable state that is still not fully understood. Hydromechanically stable state means that the effective stresses are still present in the soil layer to resist fluidisation. The unstable state means that there are no effective stresses in the layer, and the soil has fluidised after experiencing a higher number of broken contacts and zero shear resistance.

The discrete element method (DEM) is a useful tool for assessing the micromechanics of a granular medium [11, 42] that has been effectively used to study the evolution of interparticle contacts and fabric during shear using the scalar and directional parameters [3, 15, 16, 50]. In this study, the scalar parameters are chosen for the purpose of analysis since the fluidisation behaviour is closely related to scalar measurements of the fabric. The coordination number (number of contacts per particle in the granular assembly) is a fundamental microscale fabric descriptor for characterising granular medium [15, 50]. Nonetheless, the state of interparticle contacts and fabric during fluid flow has rarely been considered. In addition, the constraint ratio, defined by the ratio of the number of constraints to the number of degrees of freedom within the particle system [12], can be used to represent the relative slip and loss of interparticle contacts during instability.

The primary scope of this paper includes an attempt to describe and quantify the critical hydromechanical conditions corresponding to the fluidisation phenomenon with special attention to granular soil at the microscale, adopting the concepts of the coordination number and the constraint ratio, as mentioned above. In this context, the DEM can be combined with unresolved and resolved computational fluid dynamics (CFD) to study fluid-particle interaction in detail [6, 38, 39, 54]. Neither of these studies could accurately quantify the critical hydromechanical conditions leading to potential fluidisation from a microscale perspective, so a more insightful microscale study of this instability process is needed.

In view of the above, this study uses a combined LBM-DEM approach that is becoming increasingly popular to investigate fluid-particle interactions [4, 17, 18, 21, 29, 36, 55]. The advantages of fully resolved approaches (using LBM) over unresolved approaches include (a) the ability to generate a much finer mesh size, i.e. finer than the particles that can simulate true experimental conditions, (b) a higher computational speed when executed on parallel computers and, (c) the relative feasibility of implementation in complex geometries of porous media [19, 44]. In addition, the LBM is based on the kinetic theory of gases and represents a fluid through an assembly of particles that go through successive collision and propagation processes. This enables the calculation of

the macroscopic fluid velocity and the pressure as a function of the momentum of these particles [44, 46].

2 Lattice Boltzmann method (LBM) combined with discrete element method (DEM)

The theoretical formulations of the LBM-DEM approach are described as follows:

2.1 Fluid equations

The governing Boltzmann equation is written as [8]:

$$\frac{\partial f_{\alpha}(x, t)}{\partial t} + e_{\alpha}^v \nabla f_{\alpha}(x, t) = \Omega_{\alpha} \quad (\alpha = 1, 2, \dots, N) \quad (1)$$

where $f_{\alpha}(x, t)$ is the particle distribution function in the α direction, e_{α}^v is the microscopic fluid velocity and Ω_{α} is the collision operator, and t is the time. Equation (1) can be discretised on a regular lattice using a unique finite difference method, and the lattice Boltzmann equation with the Bhatnagar–Gross–Krook (BGK) collision operator for a Newtonian fluid is written as [5, 8]:

$$f_{\alpha}(x + e_{\alpha}^v \Delta t, t + \Delta t) - f_{\alpha}(x, t) = \Omega_{\alpha}^{\text{BGK}} \quad (2)$$

where $\Omega_{\alpha}^{\text{BGK}}$ is the BGK collision operator, and Δt is the time step.

Each time step is divided into two sub-steps, i.e. the collision and streaming step, and the collision step is written as:

$$f_{\alpha}(x, t^*) = f_{\alpha}(x, t) + \Omega_{\alpha}^{\text{BGK}} \quad (3)$$

$f_{\alpha}(x, t^*)$ and $f_{\alpha}(x, t)$ are the particle distribution functions after and before the collision, respectively, and t^* is the time after the collision. In the streaming step, the $f_{\alpha}(x, t^*)$ is propagated over the lattice grid as follows:

$$f_{\alpha}(x + e_{\alpha}^v \Delta t, t + \Delta t) = f_{\alpha}(x, t^*) \quad (4)$$

2.2 Fluid-particle interaction

The participation of solid particles in the fluid is achieved by introducing an additional collision term (Ω_{α}^s) in Eq. (3) [41]:

$$f_{\alpha}(x, t^*) = f_{\alpha}(x, t) + [1 - B] \Omega_{\alpha}^{\text{BGK}} + B \Omega_{\alpha}^s \quad (5)$$

$$B = \frac{\varepsilon_s \left(\tau / \Delta t - 1/2 \right)}{(1 - \varepsilon_s) + \left(\tau / \Delta t - 1/2 \right)} = (0, 1) \quad (6)$$

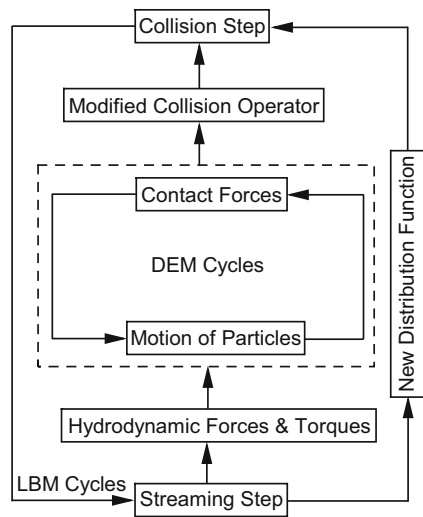


Fig. 1 Flow chart of the lattice Boltzmann method (LBM) combined with the discrete element method (DEM)

where ε_s is the solid fraction in the fluid cell volume, B is a weighting function for correcting the collision phase of the lattice-BGK equation due to the presence of solid particles, and τ is the relaxation time (Appendix 1). The method for calculating the solid fraction for the moving particles is described by Seil [45].

The non-equilibrium part of the particle distribution function is bounced back and Ω_α^s is computed using:

$$\Omega_\alpha^s = f_{-\alpha}(x, t) - f_\alpha(x, t) + f_\alpha^{\text{eq}}(\rho_f, v^p) - f_{-\alpha}^{\text{eq}}(\rho_f, u) \quad (7)$$

where v^p is the velocity of solid particle p at time $t + \Delta t$ at the node, u is the macroscopic fluid velocity, and the notation $f_{-\alpha}$ is the rebound state obtained by reversing all microscopic fluid velocities, i.e. e_α^v to $e_{-\alpha}^v$. Further details on the fluid equations and the fluid-particle interaction are described in Appendix 1.

Figure 1 shows the flow chart of the LBM-DEM approach described above. The DEM calculation cycles are within the LBM cycles. A suitable interval for the information transfer was chosen so that the accuracy of the simulation could not be impaired. The DEM code Lammmps Improved for General Granular, and Granular Heat Transfer Simulations (LIGGGHTS) was coupled with LBM code PALABOS [33, 45].

3 Simulating soil specimen fluidisation

3.1 Simulation approach

Three-dimensional LBM-DEM simulations were carried out using the Hertz-Mindlin contact model (Appendix 2)

with the Young's modulus and the Poisson's ratio of the particles as 70 GPa and 0.3, respectively [26, 50]. The particle density was set to 2650 kg/m³, and the rigid boundary walls were used. The most widely employed boundary type includes rigid boundaries with frictional walls (O'Sullivan [42]) and they have been used in the past to simulate fluidisation and internal instability (e.g. Thornton et al. [52], Nguyen and Indraratna [38], Kawano et al. [32]). Based on these past studies, frictional walls as boundary conditions have been adopted in this study. In a real soil column, the use of frictional walls considers the presence of lateral grains. Although periodic boundaries could have been used instead (e.g. Thornton [50]). Rigid frictional boundaries are often more straightforward to implement than periodic boundaries. Not examining the influence of different boundary conditions on the micromechanics of the soil sample is a limitation of the current study. The gravitational deposition method was used for sample preparation [1], whereby the acceleration due to the force of gravity of the particles was set to 9.81 m/s². The particles were initially created in a larger volume with no overlap and then dropped under gravity. The particles were allowed to settle until equilibrium was reached, thereby ensuring that the coordination number remained constant for a sufficient number of numerical cycles. The sample was prepared in a dense state by setting the coefficient of friction (μ_s) to 0 [1, 9, 26]. Subsequently, μ_s was changed to 0.30, and the particles were re-equilibrated with a sufficient number of numerical cycles before the particles became saturated with the fluid [9, 50]. The μ_s value used in this study is in the range of real quartz particle values that can be determined experimentally with a micromechanical interparticle loading apparatus (e.g. [47]). It is assumed that the particle-wall contact parameters correspond to the particle-particle contact parameters [22].

The fluid density was set to 1000 kg/m³ with a kinematic viscosity of 1×10^{-6} m²/s according to pure water properties at 20 °C and 1 atmosphere (101 kPa). The resolution of the fluid lattice was chosen with at least five lattices in each particle, i.e. the smallest particle diameter corresponds to at least five fluid cells with regard to the validation of the single particle displaced downwards into the fluid as described previously. A relaxation parameter close to but greater than 0.50 was chosen, and the Mach number was kept below 0.1, inspired by the need for improved accuracy, as explained elsewhere by Han et al. [19]. The fluid flow was initiated with the relevant inlet and outlet pressure boundary conditions, and no-slip conditions were imposed on the boundaries perpendicular to the flow. For each hydraulic gradient applied, the flow was continued over a sufficient period of time until a steady-state condition was attained. The flow was initiated in the upward direction with the gravity of the particles on.

3.2 Particle size distribution and homogeneity of the sample

Figure 2a shows the particle size distribution of the selected sample from an experimental study carried out by Indraratna et al. [28]. Figure 2b shows the three-dimensional DEM-based sample with 17,607 particles, and the direction of flow of the fluid is also shown, i.e. the z -direction. Mud pumping and fluidisation occur owing to the upward flow induced by the excessive hydraulic gradient (e.g. Indraratna et al. [27, 28]), which is why the authors have chosen the z -direction (upward direction) for simulation purposes. Figure 2c shows the division of the sample into ten different inner layers. The ratio of the lateral dimension of the simulation domain to the maximum particle diameter was kept greater than 12 in order to obtain a representative elementary volume (REV) and avoid the boundary effects. A local increase in the void ratio occurs near the rigid boundaries [42]; hence, the bottom boundary layer (besides the rigid bottom boundary) was neglected in order to nullify the boundary effects [23]. The thickness of each layer was chosen to be more than twice the maximum particle diameter to define a REV [23]. The stresses at the boundaries do not reflect the actual material response; therefore, the interaction of the particles in each layer with the lateral boundaries was not taken into account.

Figure 2c shows the similar initial void ratios of all layers, indicating the REV in each layer, and the initial homogeneity of the sample was further confirmed by considering the variances in the void ratios as reported by Jiang et al. [31]:

$$S^2 = \frac{1}{n_L - 1} \sum_{k=1}^{n_L} (e_{oi}^k - e_{oi}^{avg})^2 \quad (8)$$

where S is the variance of the void ratios, n_L is the total number of layers, e_{oi}^k is the initial void ratio of the k th layer, and e_{oi}^{avg} is the initial void ratio of the entire sample. The S^2 value for the sample in Fig. 2c is 2.72×10^{-5} , which is sufficiently low to classify the sample as homogenous with respect to the REV in each layer. The overall void ratio of the numerical sample is the same as that of the experimental sample. Note that the void ratio does not take into account the particulate structure of the granular medium. Figure 2d shows a close-up view of the particles modelled in the fluid mesh. It can be seen that the mesh size is much smaller than the particle and pore size, in contrast to the conventional unresolved approach with the Navier–Stokes equation.

3.3 Calibration

Fluid and grain densities were determined from previous experimental investigations carried out earlier by the authors (Indraratna et al. [28]), and the contact friction angle was chosen from previous DEM studies on similar granular materials (e.g. Sufian et al. [48]). Since the above parameters were determined at the initial stage, the relaxation time (τ) was then obtained during the calibration process. Figure 3a shows the calibration of the relaxation time (τ) for soil fluidisation by comparing the pressure drops obtained from the LBM-DEM approach and an analytical solution (Ergun [14]). For further analysis, a relaxation time (τ) = 0.56 was chosen, and this is in-line with the appropriate value of the kinematic viscosity of the water as used in the experiments. Figure 3b compares the flow curves obtained from the LBM-DEM approach and an earlier experimental study [28]. The flow curves obtained from the LBM-DEM approach and experimental methods agree. The overall critical hydraulic gradient ($i_{o,cr}$) refers to the gradient at which the effective stresses drop to zero, and the soil becomes fluidised. $i_{o,cr}$ predicted by the LBM-DEM approach was 1.050, while the experimental value of $i_{o,cr}$ was 1.180. These values are in reasonable agreement with each other. This acceptable agreement with the experimental results implies that the lattice resolution of five fluid cells per particle is sufficient to capture the fluidisation behaviour of the particle size distribution considered in this study. Nevertheless, in complex LBM-DEM modelling such as this, where a huge number of particles of different sizes and shapes cannot be accommodated to represent an ideal real-life pore structure or void distribution due to the obvious computational challenges, one cannot guarantee perfect accuracy; this is recognised as a current limitation to be further improved in the future.

4 Results and discussion

4.1 Stress-hydraulic gradient evolution

Figure 4a shows the evolution of overall hydraulic gradient over time. Figure 4b shows the stress-hydraulic gradient space where the local hydraulic gradients (i_{hyd}) are plotted against the normalised Cauchy effective stresses ($\sigma'_{zz}/\sigma'_{zz0}$) of particles in a given layer in the fluid flow direction (vertical direction) at any time, where σ'_{zz} is the Cauchy effective stresses of the particles in a layer at any time, and σ'_{zz0} is the initial Cauchy effective stresses of the particles in that particular layer. The σ'_{zz} is obtained using the particle-based stresses via the following second-order stress tensor equation [43].

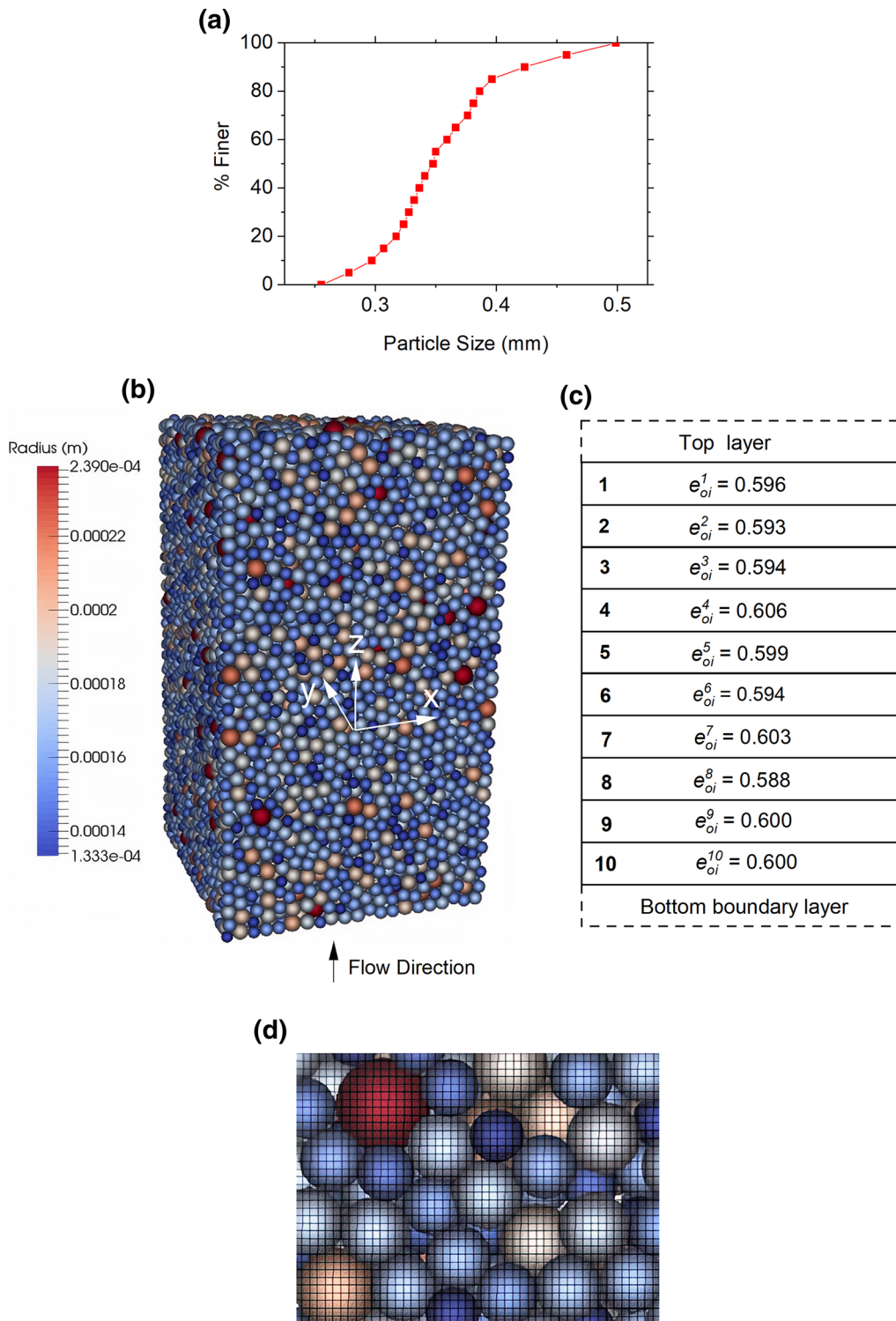


Fig. 2 **a** Particle size distribution of the sample selected for modelling in DEM; **b** three-dimensional sample modelled in DEM; **c** division of the sample into different layers with the mentioned layer numbers and initial void ratios (e_{oi}); **d** a close-up view of the particles modelled in the fluid mesh using the LBM-DEM approach

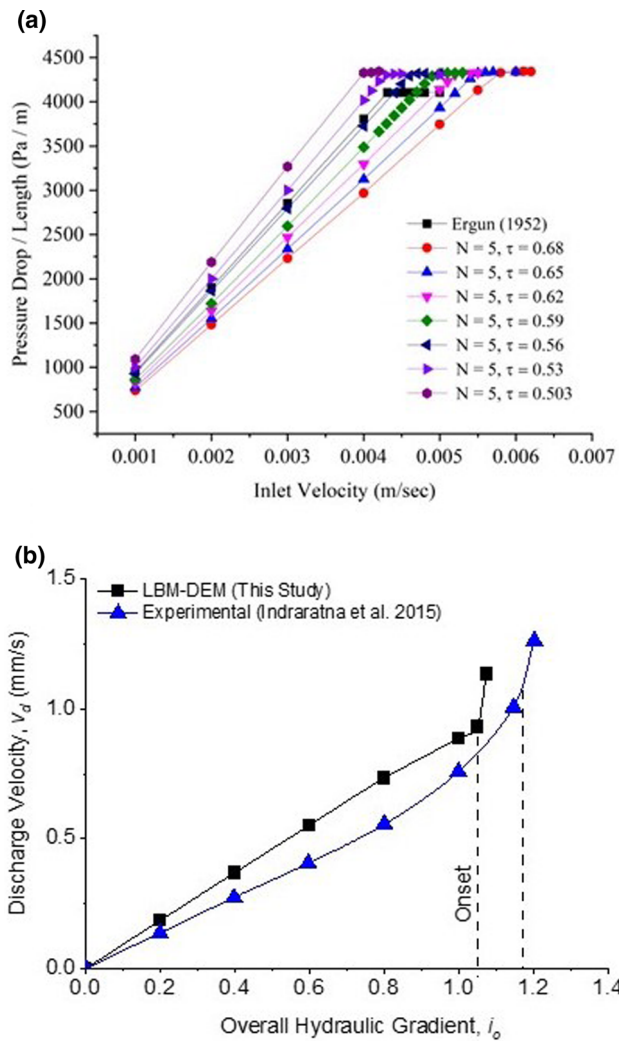


Fig. 3 **a** Calibration of the relaxation parameter by comparing the pressure drops obtained from the LBM-DEM and an analytical solution, **b** comparison of the flow curves obtained from the LBM-DEM and the documented experimental work

$$\sigma'_{ij} = \frac{1}{V} \sum_{p=1}^{N_p} \sigma_{ij}^{p'} V^p \tag{9}$$

where V is the volume of the layer or the selected region, V^p is the volume of particle p in the region, N_p is the number of particles in the layer, and $\sigma_{ij}^{p'}$ is the average stress tensor within a particle p and is given by:

$$\sigma_{ij}^{p'} = \frac{1}{V^p} \sum_{c=1}^{N_c^p} |x_i^c - x_i^p| n_i^{c,p} f_j^c \tag{10}$$

where f_j^c is the force vector in the j th direction at contact c with the location x_i^c , x_i^p is the location of the particle's centroid, $n_i^{c,p}$ is the unit normal vector from the particle's centroid to the contact location and N_c^p is the number of contacts on the particle p . Note that Eqs. (9) and (10)

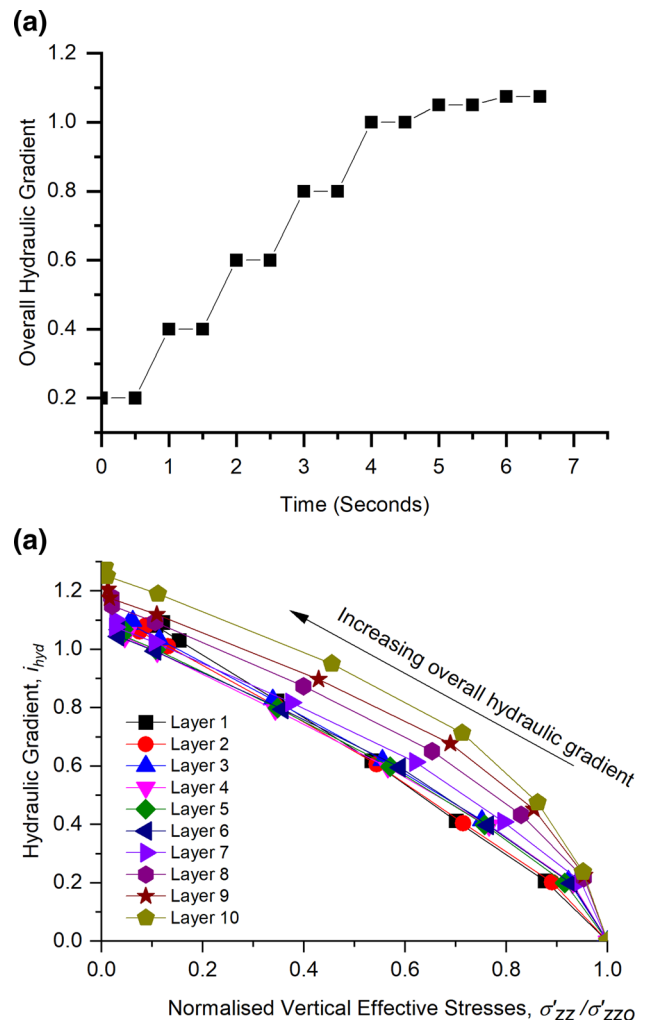


Fig. 4 **a** Evolution of overall hydraulic gradient with time; **b** evolution of the increasing local hydraulic gradient (i_{hyd}) and the decreasing normalised effective stresses ($\sigma'_{zz} / \sigma'_{zso}$) (for each layer, the eight symbols correspond to the initial state and the seven increase in the overall hydraulic gradient (a))

compute the effective stresses directly from the contact moments and not according to Terzaghi's concept used in the macroscale laboratory studies. Reynold's stresses are negligible and are not taken into account.

Figure 4b shows that the onset of fluidisation of the soil is associated with hydraulic and stress conditions, i.e. hydromechanical conditions. The effective stresses decrease with increasing local hydraulic gradients in each layer. The onset occurs at a critical hydraulic gradient when the effective stresses drop to zero. The evolution of the stress-gradient of each layer is not the same. The stress-gradient paths of Layers 1–6 are approximately linear with a slope of -1 . In contrast to the theoretical linear stress-gradient paths presented by Li and Fannin [35], the stress-gradient paths of Layers 7–10 (lower layers) are nonlinear until failure. The failure initiates when the effective stress

of Layer 10 approaches zero. At the same time, Layers 1–9 show residual stresses due to the motion of the particles in the form of clusters. These residual stresses decrease as the particles in the cluster would lose further contacts over time after onset until complete fluidisation occurs.

Lateral (horizontal) stresses did not affect fluidisation in the current study, as the ratio between the horizontal and vertical stresses was always less than 1 at the hydrostatic state and before fluidisation (see Fig. 5a, b). The effective horizontal stresses (due to increased water pressure) decrease to zero, so it is the vertical stresses that predominantly control the onset of fluidisation (Fig. 5b). In this respect, there is no possibility of any arching effect when approaching the state of fluidisation, and only the vertical stresses should be considered when quantifying soil fluidisation. In real-life situations, the observed instability of shallow soil deposits (e.g. mud pumping under

cyclic train loading) has also proven that the ratio of effective lateral to vertical stresses in the field is smaller than unity.

4.2 Broken contacts

Figure 6 shows the development of the broken contacts (B_R) compared to the normalised effective stresses ($\sigma'_{zz}/\sigma'_{zz0}$). B_R is the percentage of interparticle contact losses in the initial number of contacts in the corresponding layer. The value of B_R increases with increasing hydraulic gradient and decreasing effective stresses. Contact is lost when the normal contact force due to hydrodynamic forces becomes zero. When the fluid flows, the contacts break off, and new contacts are also formed in the layer. The sharp turn in B_R represents the critical hydromechanical state where the contacts are notably lost. The granular assembly would become a fully fluid-like material when the number of unconnected particles increases to the maximum due to the breakage of the contacts, i.e. most of the particles would simply float without any contact. It can also be seen that the contact losses in the lower layers are greater than in the upper layers, which shows that more particles lose contact at the bottom and migrate upwards with the fluid flow if the constrictions are wide enough. The B_R at the critical hydraulic gradient is about 5% in Layer 1 and 17% in Layer 10 and increases considerably with a further slight increase in the hydraulic gradient applied across the soil specimen. The bottom layer has a higher percentage of broken contacts because the local hydraulic gradient is higher in the bottom layer than in the top layer. This difference in local hydraulic gradients is attributed to

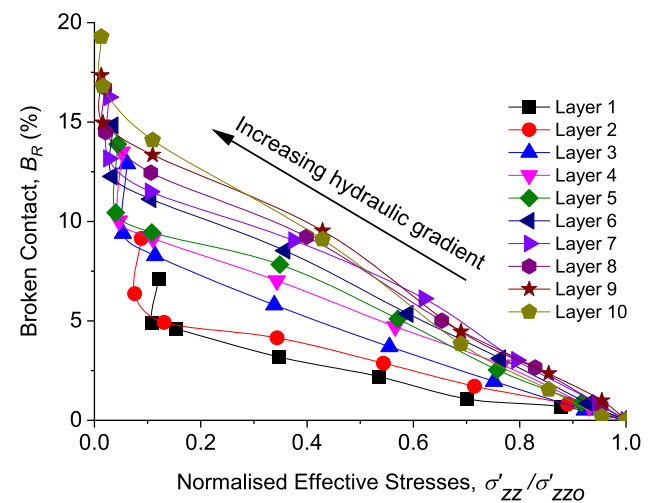
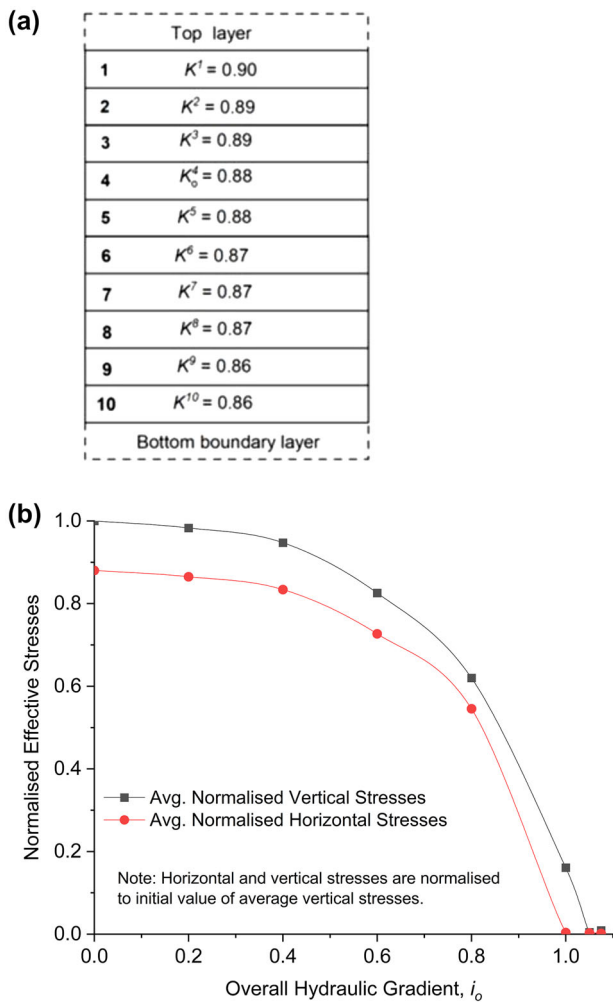


Fig. 5 a Division of the sample into different layers with the indicated layer numbers and coefficient of earth pressure (K) values at the hydrostatic state, b development of the normalised horizontal and vertical effective stress with hydraulic gradient

Fig. 6 Evolution of increasing broken contacts (B_R) with the decreasing normalised effective stresses ($\sigma'_{zz}/\sigma'_{zz0}$) (for each layer, the eight symbols correspond to the initial state and the seven increase in the overall hydraulic gradient (Fig. 4a))

anisotropy in the contact and pore networks due to gravity deposition. The microscale parameters considered in this study can be determined in the field where the variations in hydraulic gradients, effective stresses and void ratios can be predicted, and then used to back-calculate these microscale parameters.

4.3 Mechanically stable particles

Figure 7 shows the evolution of the fraction of mechanically stable particles (M_s) with normalised effective stresses ($\sigma'_{zz}/\sigma'_{z0}$) under increasing hydraulic gradients. The mechanically stable particles are those that participate in the stable network of force transmission. The value of M_s is defined by [25]:

$$M_s = \frac{N_p^{\geq 4}}{N_p} \tag{11}$$

where $N_p^{\geq 4}$ is the number of particles with at least 4 or more contacts. Particles with zero contacts that do not participate in the stable network of force transmission are called rattlers or unconnected particles; hence, they are excluded. The particles with 1, 2, and 3 contacts are temporarily stable for a limited time, so they are also neglected in the above equation.

It should be noted that the values of M_s are always smaller than 1 across all layers since the temporarily stable particles are also present at the hydrostatic state. The initial values of M_s are higher in the lower layers than in the upper layers. The values of M_s decrease across all layers with a decrease in the values of the effective

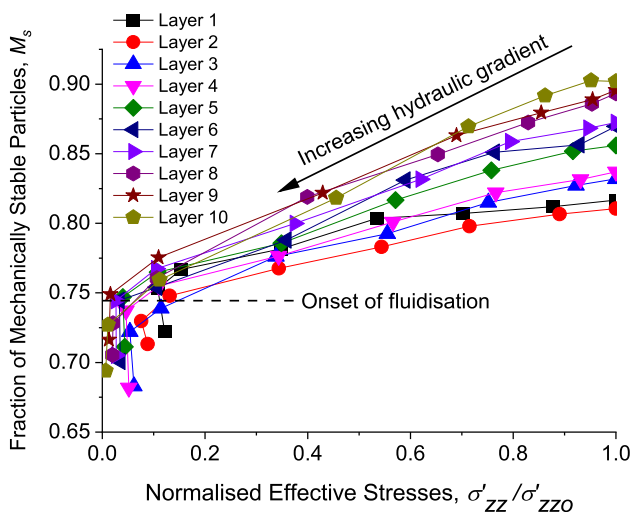


Fig. 7 Development of the decreasing fraction of mechanically stable particles (M_s) with decreasing normalised effective stresses ($\sigma'_{zz}/\sigma'_{z0}$) (For each layer, the eight symbols correspond to the initial state and the seven increase in the overall hydraulic gradient (Fig. 4a))

stresses. This reduction becomes significant at the critical hydraulic and stress conditions that indicate the break-up of the clusters of mechanically stable particles. The results show that a critical value of $M_s \approx 0.75$ is found for all layers, below which the fluid-like behaviour of the soil is observed.

4.4 Evolution of the soil fabric

Figure 8 shows a conceptual model that describes the differences in the fabrics of two-particle systems where particles with two different geometrical arrangements are placed. Note that the void ratios of both arrangements are the same. However, the number of interparticle contacts is different due to the dissimilarity of the fabrics of the particulate systems. It is noteworthy that the geometric arrangement of the particles is more important than the void ratio when it comes to the strength of the granular assembly [12]. Similar initial void ratios of all layers indicate that the number of particles in each layer is the same. However, the number of interparticle contacts can vary due to the different geometrical configurations of the particles. During fluid flow, the number of particles in each layer remains unchanged until fluidisation begins, while the geometrical re-arrangement of the particles can occur, mainly due to the fact that the interparticle contacts within the layer slip and/or break.

To assess the evolution of soil fabric under fluid flow, this study uses a scalar approach (e.g. Fonseca et al., 2013) to quantify the fabric with a scalar fabric descriptor called the coordination number (Z) and is computed as follows [50].

$$Z = \frac{2N_c}{N_p} \tag{12}$$

where N_c is the number of contacts and is multiplied by 2 since each contact is shared by two different particles. The coordination number is a basic descriptor to quantify the

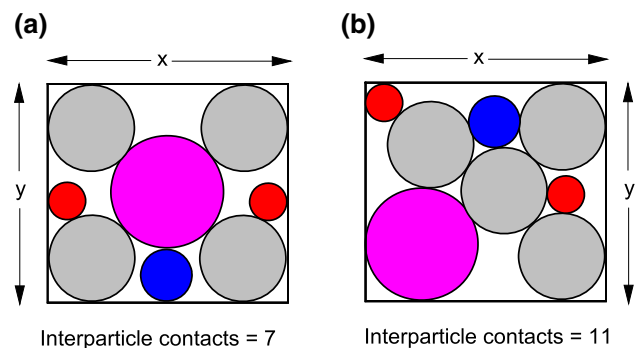


Fig. 8 Conceptual model showing the differences in the fabrics of particles with the same void ratios

fabric, and the non-application of more advanced approaches is a limitation of this study.

Figure 9 shows the distribution of the Z at the hydrostatic state and the onset of soil fluidisation, taking into account three distinct cases:

(a) all particles

- (b) particles with diameters (d_p) $\geq d_{50}$ (where d_{50} is the particle size that is 50% finer by mass), and
- (c) particles with $d_p \geq d_{85}$ (where d_{85} is the particle size that is 85% finer by mass).

Despite the narrow range in the particle size distribution curve, the difference in the coordination number distribution becomes clearer when the conditions $d_p > d_{50}$ and

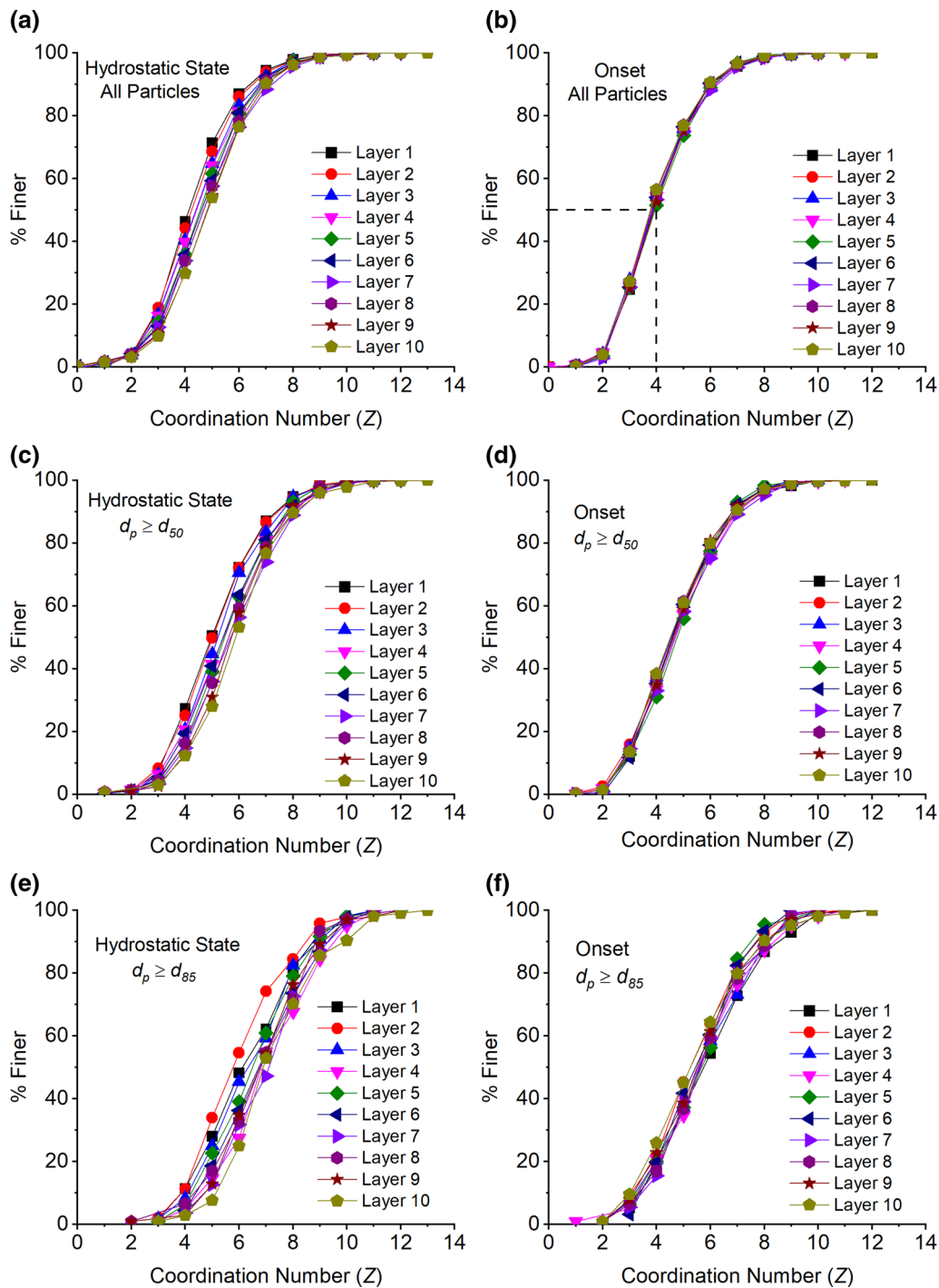


Fig. 9 Cumulative distributions of the coordination number (Z) at the hydrostatic state and the onset of fluidisation of soil specimen

$d_p > d_{85}$ are applied. Therefore, it is essential to consider all cases.

Figure 9a shows that the distribution of the coordination numbers at the hydrostatic state across different layers is somewhat dissimilar when all particles are considered. This difference is enhanced when the larger particle sizes are taken into consideration (Fig. 9c, e), which shows a dissimilarity in the fabric of all layers despite the similar void ratios. This fabric dissimilarity is ascribed to the influence of gravity during the sample preparation phase. The curves of the lower layers are on the right-hand side and show higher values of the coordination numbers than those of the upper layers. The slight difference in the evolution of local hydraulic gradients and effective stresses through each layer, as previously described, is due to this slight dissimilarity of the particles' fabric in the layers. It is appealing to note that at the onset of fluidisation, the distributions of the coordination numbers of all layers converge and become similar (Fig. 9b, d, f). The median value of the coordination number (Z_{50}) is 4 when all particles in the granular medium of the layer are taken into account (Fig. 8b). Thus, at the onset of fluidisation, the distributions of the interparticle contacts are uniform and show a similar fabric for all soil layers.

Figure 10 shows average coordination numbers (Z_{avg}) versus normalised effective stresses ($\sigma'_{zz}/\sigma'_{zso}$), where the initial (at the hydrostatic state) average coordination of Layer 10 is the highest (i.e. $Z_{avg} = 5.405$), while Layer 1 has the lowest (i.e. $Z_{avg} = 4.811$). As the normalised effective stresses decrease, the values of Z_{avg} decrease across all layers, and so does the difference between them. Although each layer initially had a different fabric, the Z_{avg}

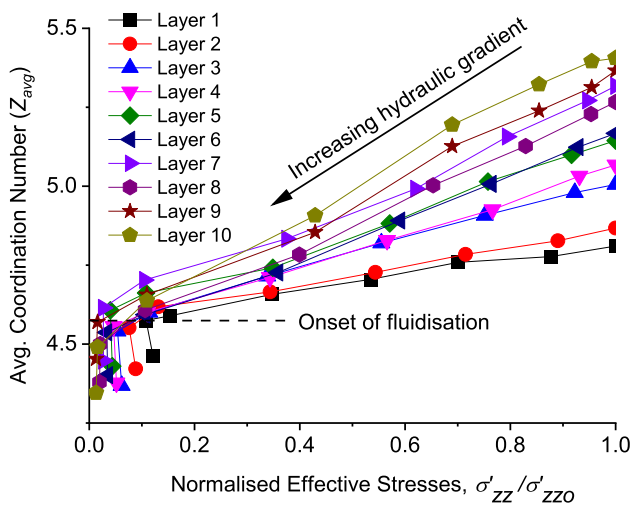


Fig. 10 Development of the decreasing average coordination number (Z_{avg}) with decreasing normalised effective stresses ($\sigma'_{zz}/\sigma'_{zso}$) (For each layer, the eight symbols correspond to the initial state and the seven increase in the overall hydraulic gradient (Fig. 4a))

of all layers has evolved to become the same, i.e. 4.6 at critical hydromechanical state.

4.5 Sliding index

Figure 11 shows the distribution of the sliding index (S_i) of the selected Layer 10. Note that all layers show an almost similar development in the sliding index as the local hydraulic gradient increases. The sliding index (S_i) is defined by [25]:

$$S_i = \frac{f^T}{\mu_s f^N} \tag{13}$$

Sliding or the plastic contacts occur when the tangential contact force (f^T) has fully mobilised the friction, i.e. $S_i = 1$. The contacts with $S_i < 1$ are the elastic contacts and f^T is independent of f^N in such contacts. Note that contacts that have already been lost are not taken into account when calculating S_i .

The results show that a small proportion of the contacts slide even at the hydrostatic state since the static buoyancy forces would be acting on the particles when they are saturated with the fluid. As the local hydraulic gradients increase, the elastic contacts decrease, and the sliding contacts increase. The hydrodynamic forces from the seepage flow tend to move the particles, causing a change in the magnitudes of the resisting tangential contact force and the normal contact force. As a result, a slip is caused when the elastic tangential contact force reaches the Coulomb cut-off, i.e. $f^T = \mu_s f^N$. Two types of contact networks are present, strong and weak contacts. Strong and weak contact forces are defined for each layer with respect to the mean contact force in each corresponding layer. The strong contacts that carry the primary load are those with above-average normal contact forces; otherwise, they correspond to weak contacts (Thornton and Antony [51]), and this sliding of the particles occurs in the weak contacts [10]. At $i_{hyd} \leq 1$, the proportion of sliding contacts in the total number of contacts in the layer is $\leq 10\%$, while it is around 17% at the critical $i_{hyd} = 1.251$ (Fig. 11g). Thereafter, this proportion of sliding contacts increases steeply with a further, albeit slight, increase in the hydraulic gradient. It is noteworthy that the maximum tangential force is controlled by the value of μ_s . Therefore, the value of μ_s has a profound influence on the proportion of sliding contacts and consequently on the macroscale behaviour of the granular assembly.

4.6 Constraint ratio

Figure 12 shows a three-dimensional representation of the constraint ratio (R) versus local hydraulic gradients (i_{hyd})

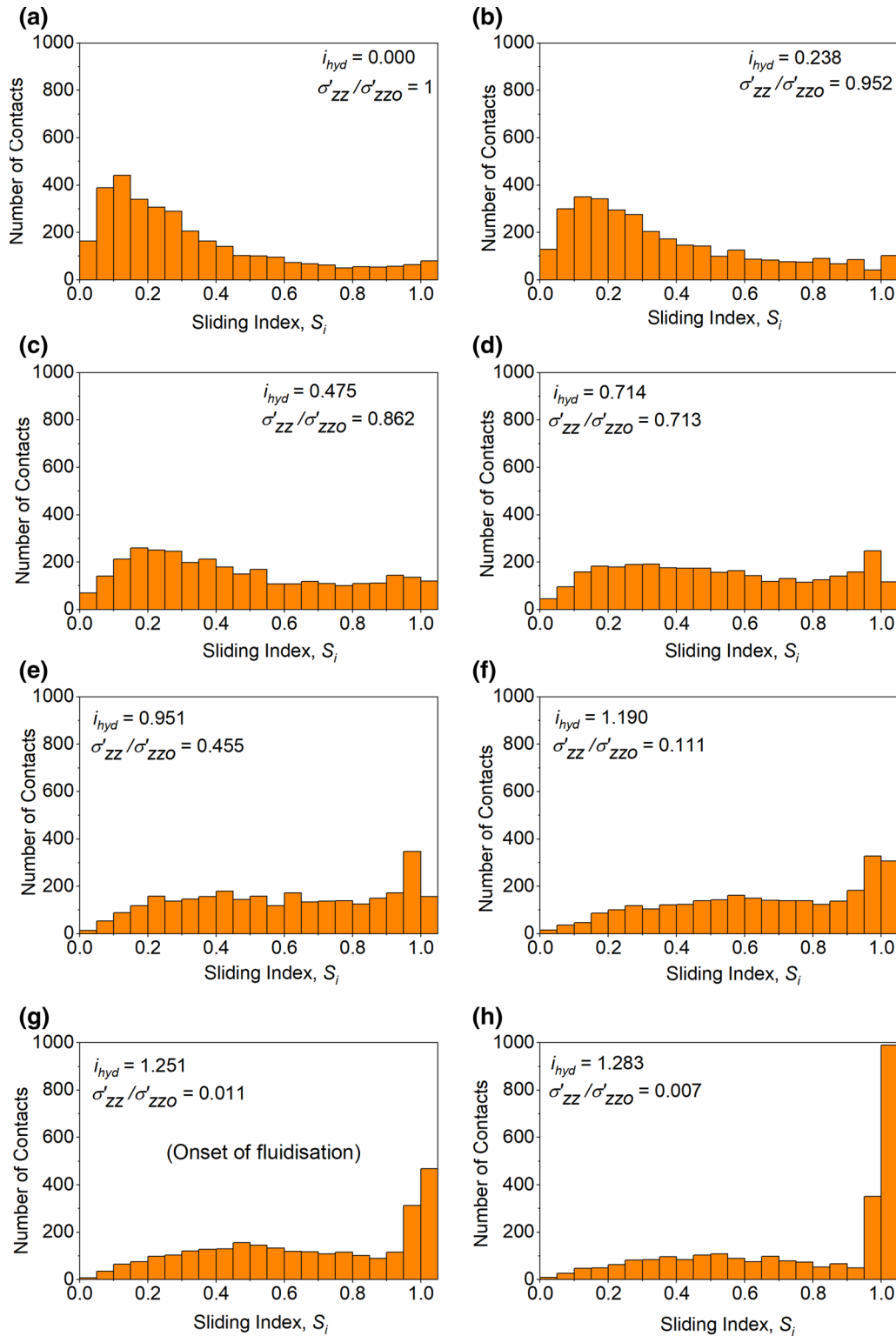


Fig. 11 Distribution of the sliding index (S_i) of the selected Layer 10 with different local hydraulic gradients (i_{hyd})

and normalised effective stresses ($\sigma'_{zz}/\sigma'_{zZo}$). The constraint ratio for a three-dimensional particle system that only takes the sliding resistance into account is given by [12]:

$$R = \frac{N_{ct}}{N_d} = \frac{N_c(3 - 2S_c)}{6N_p} \tag{14}$$

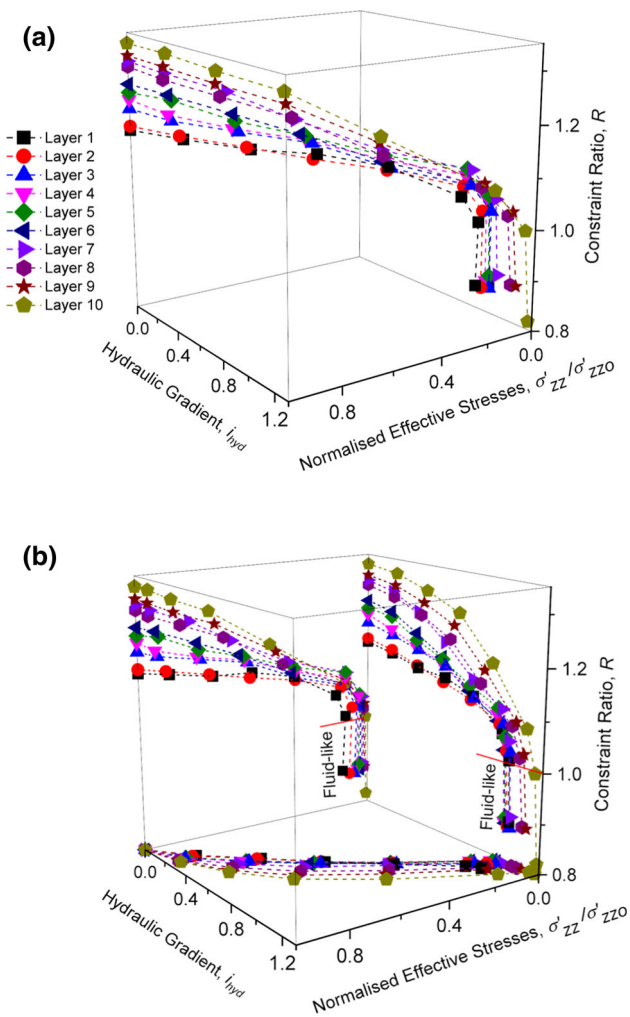


Fig. 12 (a) Three-dimensional representation of the hydraulic gradient (i_{hyd}), the normalised effective stresses ($\sigma'_{zz}/\sigma'_{zz0}$), and the constraint ratio (R); (b) projections of the three-dimensional plot of i_{hyd} , $\sigma'_{zz}/\sigma'_{zz0}$, and R (for each layer, the eight symbols correspond to the initial state and the seven increase in the overall hydraulic gradient (Fig. 4a))

where N_{ct} is the number of constraints, N_d is the number of degrees of freedom, and S_c is the fraction of slipping contacts in the total number of contacts at a given point in time. For an idealised granular medium with $\mu_s = \infty$, $N_{ct} = 3N_c$ and $N_d = 6N_p$. The realistic granular medium, however, would have a finite value of μ_s ; therefore, the two tangential force constraints on contacts subject to slipping vanish and are excluded from the total number of constraints given in Eq. (14). Theoretically, if $N_{ct} > N_d > N_d$, the granular assembly is considered to be over-constrained or mechanically stable, and if $N_{ct} = N_d$, it is considered to be in a critical or transitional state; otherwise, it is unstable. Note that R represents both slipping and loss of contacts in the particle systems, whereas the coordination number [50] does not take into account the slipping of particles.

The constraint ratio in each layer decreases according to the nonlinear power laws when the normalised effective stresses decrease, and it decays exponentially after the onset of the soil fluidisation (Fig. 12). The initial mild slope shows that at the relatively low i_{hyd} values, i.e. $i_{hyd} < 1$, the particles slip less and have minimal loss of contacts. The abrupt change in slope after onset is triggered by substantial slipping and the associated rapid loss of interparticle contacts. The point at which the slope value changes represents the critical microscale hydromechanical state or the onset of soil fluidisation. This point is marked as a transition line from a hydromechanically stable to a fluid-like state, as shown in Fig. 12b. This critical hydromechanical state corresponds to $R \approx 1$, with effective stresses ≈ 0 at the critical hydraulic gradient. Therefore, the soil is hydromechanically stable when R is greater than 1. It is in a transition state from a hydromechanically stable to a fluid-like state when R is 1; otherwise, it corresponds to a slurry or fluid-like state. Complete fluidisation of the soil specimen occurs when almost all interparticle contacts are lost, with a constraint ratio well below 1.

5 Conclusions

This study assessed the hydromechanical state of soil fluidisation from a micromechanical perspective using the LBM-DEM approach. The good agreement between the model predictions and the experimental observations in relation to particle motion, fluid flow curves, and the critical hydraulic gradients confirms the capability and reliability of this hybrid numerical method. Based on the findings of this study, the following salient outcomes can be drawn:

- At comparatively low values of the local hydraulic gradient (i_{hyd}), i.e. $i_{hyd} \leq 1$, the proportion of slipping contacts in the total number of contacts of the selected Layer 10 (bottom of the specimen) was $\leq 10\%$, while it was approximately 17% at the critical $i_{hyd} = 1.251$. The extent of slipping contacts increased with a further increase in the hydraulic gradient applied across the soil specimen.
- The fraction of mechanically stable particles was generally larger at the deeper layers but decreased with the reduction in normalised effective stress during the corresponding increase in hydraulic gradient. The fluid-like state of soil was triggered when this fraction of mechanically stable particles dropped below 0.75.
- The hydrodynamic forces induced by the seepage flow inevitably destabilize and move the particles within the granular assembly, resulting in reduced contact forces, thus creating critical conditions to facilitate particle slipping. The loss of interparticle contacts was not uniform across the depth of the soil specimen, as this

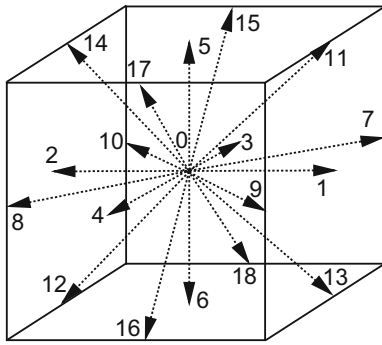


Fig. 13 Directions of the 19 (0–18) velocity vectors of the *D3Q19* discretisation scheme used in this study

was more pronounced in the deeper layers when subjected to an upward flow from the base of the specimen.

- At the critical hydraulic gradient, the percentage of interparticle contact losses relative to the initial number of contacts was non-uniform and varied between 5 and 17% across the specimen depth. After that, even with a slight increase in the hydraulic gradients, the breakage of the interparticle contacts appeared to exacerbate.
- At the onset of fluidisation, the distributions of the coordination numbers across all layers of the soil specimen became more uniform, with a median value of 4 and an average value of 4.6, thus representing a more uniform granular fabric across the soil layers.
- The constraint ratio (ratio of the number of constraints to the number of degrees of freedom in the particle system) was used to distinguish hydromechanically stable and unstable states. A value of the constraint ratio greater than 1 represented the hydromechanically stable state and less than 1 the unstable state. The critical hydromechanical state was found at a constraint ratio of unity. Constraint ratio represented the slippage and loss of contacts in the particle system, and its value decreased with the increase in the hydraulic gradient. The slipping and the associated loss of contact between the soil particles would cause the effective stresses to drop. This implies from a microscale perspective that soil fluidisation could be triggered by excessive slippage and the inevitable loss of contacts between particles.

Appendix 1: LBM-DEM approach

The Ω_x^{BGK} , through which the momentum transfer occurs between the fluid particles when they collide, is given by [5]:

$$\Omega_x^{BGK} = -\frac{\Delta t}{\tau} (f_x(x, t) - f_x^{eq}(x, t)) \tag{15}$$

where $f_x^{eq}(x, t)$ is the equilibrium distribution function, τ is the relaxation time, and is related to the kinematic viscosity (ν_f) of the fluid, the lattice spacing (Δx), and the time step (Δt) by the following relationship:

$$\nu_f = \frac{1}{3} \left(\tau - \frac{1}{2} \right) \frac{\Delta x^2}{\Delta t} \tag{16}$$

Equation (16) implies that the τ value should be greater than 0.5. For a given value of ν_f and τ , the Δt is defined according to the chosen Δx by:

$$\Delta t = \frac{1}{3\nu_f} \left(\tau - \frac{1}{2} \right) \Delta x^2 \tag{17}$$

The $f_x^{eq}(x, t)$ for the BGK model is given by [5]:

$$f_x^{eq}(x, t) = \omega_x \rho_f \left(1 + \frac{3}{c_L^2} e_x^v u + \frac{9}{2c_L^4} (e_x^v u)^2 - \frac{3}{2c_L^2} u^2 \right) \tag{18}$$

where ω_x is the weighting factor for the velocity vectors, ρ_f is the fluid density, e_x^v is the microscopic fluid velocity, u is the macroscopic fluid velocity, and $c_L c = \frac{\Delta x}{\Delta t} c = \frac{\Delta x}{\Delta t}$ is the lattice speed given by:

$$c_L = \frac{\Delta x}{\Delta t} \tag{19}$$

In lattice Boltzmann computations, $c_L = \Delta x = \Delta t = 1$, and the discretisation schemes in LBM are labelled as *DdQq*, where d is the number of dimensions, and q represents the number of velocity vectors. This study used the *D3Q19*, a three-dimensional scheme with 19 velocity vectors, including one at rest. Figure 13 shows the directions of the velocity vectors (e_x^v) for the *D3Q19* scheme and, for the sake of simplicity, their magnitudes are already defined by:

$$e_x^v = \begin{cases} (0, 0, 0) & i = 0 \\ (\pm c_L, 0, 0), \\ (0, \pm c_L, 0), (0, 0, \pm c_L) & i = 1, 2, 3, 4, 5, 6 \\ (\pm c_L, \pm c_L, 0), \\ (\pm c_L, 0, \pm c_L), \\ (0, \pm c_L, \pm c_L) & i = 7, 8, 9, 10, 11, \dots, 18 \end{cases} \tag{20}$$

and the weighing factors are $\omega_0 = 1/3$, $\omega_{1,2,3,4,5,6} = 1/18$ and $\omega_{7,8,\dots,18} = 1/36$.

The macroscopic fluid properties, i.e. fluid density (ρ_f) and velocity (u), can be retrieved at each node and given by [18, 46]:

$$\rho_f(x, t) = \sum_{\alpha=0}^{q-1} f_{\alpha}(x, t) \tag{21}$$

$$u(x, t) = \frac{1}{\rho_f} \sum_{\alpha=0}^{q-1} f_{\alpha}(x, t) e_{\alpha}^v \tag{22}$$

To determine the fluid pressure p_f , it is assumed that the fluid is slightly compressible, and the following state equation is used:

$$p_f = c_s^2 \rho_f \tag{23}$$

where c_s is the sound celerity and is defined by:

$$c_s = \frac{c_L}{\sqrt{3}} \tag{24}$$

Fluid modelled with LBM requires a slight variation in spatial density. An approximate incompressibility situation can only be achieved under the condition that the Mach number (M) is small; is therefore kept below 0.1 [19], and is defined by:

$$M = \frac{u_{\max}}{c_L} \tag{25}$$

u_{\max} is the maximum velocity in the fluid flow in physical units. Fluids with lower viscosity and turbulent flows can also be simulated with LBM using the Smagorinsky Large Eddy Simulation approach [20, 46]. Unit conversion between physical and lattice units is explained elsewhere by Latt [34].

For the fluid-particle interaction, the force (f_f) (without the static buoyancy force) and the torque (T_f) acting on a particle through the fluid can then be computed by [41, 46]:

$$f_f = \frac{\Delta x^3}{\Delta t} \left[\sum_n B_n \sum_{\alpha} \Omega_{\alpha}^s e_{\alpha}^v \right] \tag{26}$$

$$T_f = \frac{\Delta x^3}{\Delta t} \left[\sum_n B_n (x^n - x^p) \sum_{\alpha} \Omega_{\alpha}^s e_{\alpha}^v \right] \tag{27}$$

B_n is the weighting function in the cell, x^n is the coordinate of the lattice cell, and x^p is the centre of mass of the particle. Equation (27) does not include the static buoyancy forces; therefore, they are applied separately to the particles and the total hydrodynamic force (f_{hyd}) on the particle, including the static buoyancy force (f_{bu}) is given by:

$$f_{hyd} = f_f + f_{bu} \tag{28}$$

The governing equations of motion of solid particles given by Cundall and Strack (1979), with the additional fluid-particle interaction force and the torque, are as follows:

$$m^p \frac{dv^p}{dt} = f_g^p + f_{hyd}^p + \sum_{c=1}^{N_c^p} f_j^c \tag{29}$$

$$I^p \frac{dw^p}{dt} = T_f^p + \sum_{c=1}^{N_c^p} T_j^c \tag{30}$$

where m^p and I^p are the mass and the moment of inertia of the particle p , v^p and w^p are the translational and angular velocities of the particle p , N_c^p is the total number of contacts on the particle p , f_j^c is the contact force vector in the j th direction at contact c on the particle p , T_j^c is the torque that acts on the particle p due to the tangential contact force at contact c , and f_g^p is the gravitational force on the particle p .

Validation

Although LBM-DEM was previously validated by Indraratna et al. [29] with experimental observations of fluidisation, the transient motion of the particles in the fluid could not be quantified. In this regard, an attempt is made in this study to validate the motion of a single particle falling into the fluid with different particle Reynold’s numbers (Re_p). This validation is carried out by comparing the numerical results with the experimental observations by Ten Cate et al. [49]. Figure 14a, b shows the schematic sketch and the modelled problem using the LBM-DEM approach, respectively. Table 1 shows the fluid properties used with lattice resolution (N) = 5 (particle diameter corresponds to 5 fluid cells) and the relaxation time (τ) = 0.53. It is noteworthy that $N = 5$ was chosen after a preliminary sensitivity analysis in which the simulation was run with $N = 5, 7$ and 10. The results showed insignificant difference in the numerical output when $N > 5$. Figure 14c, d shows an excellent agreement between the numerical and experimental results of the position and velocity of the falling particle over time at different Reynold’s numbers. Hence, it could be justified with confidence that the LBM-DEM approach would reasonably predict the transient motion of the particles in the fluid with these selected numerical parameters, i.e. $N = 5$ and $\tau = 0.53$.

Appendix 2: Hertz-Mindlin contact model

Figure 15 shows the rheological scheme and schematic sketch of the Hertz-Mindlin contact model used in this study to simulate the fluidisation of the soil. The normal contact force (f^N) is based on Hertzian contact theory and the tangential contact force (f^T) is based on the work of Mindlin and Deresiewicz [37]. The f^N and f^T have the nonlinear spring and damping components. The normal and tangential damping coefficients (c_n and c_t) are related to the

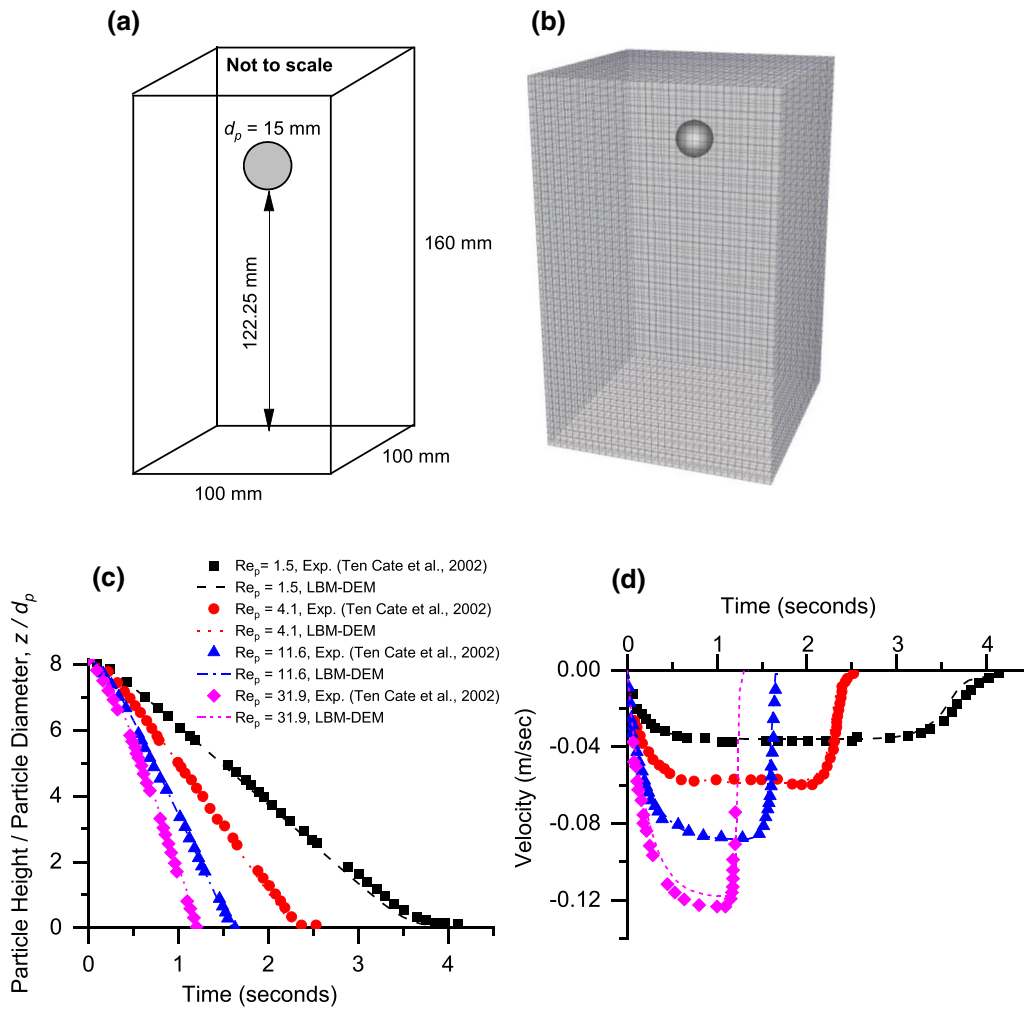


Fig. 14 **a** Schematic representation of a single sphere falling into the fluid with a diameter (d_p) = 15 mm; **b** the modelled particle in the fluid mesh using LBM-DEM; **c** comparison of the numerical and experimental results of particle position over time; **d** comparison of experimental and numerical results of particle velocity over time

Table 1 Fluid properties for simulating the single-particle falling into the fluid using the LBM-DEM approach (after Ten Cate et al. [49])

Case	Density (ρ_f) (kg/m ³)	Kinematic viscosity (ν_f) (m ² /s)
$Re_p = 1.5$	970	3.845×10^{-4}
$Re_p = 4.1$	965	2.197×10^{-4}
$Re_p = 11.6$	962	1.175×10^{-4}
$Re_p = 31.9$	960	6.042×10^{-5}

restitution coefficient as reported by Tsuji et al. [53]. The tangential frictional force follows Coulomb’s law of friction (e.g. [11]).

$$f^N = k_n \delta_n - c_n v_n^{rel} \tag{31}$$

where k_n is the elastic constant for normal contact, c_n is the viscoelastic damping constant for normal contact, δ_n is the

normal component of the displacement at the contact as represented by the overlap distance, v_n^{rel} is the normal component of the relative velocity of two spherical particles, and k_n is given by:

$$k_n = \frac{4}{3} E^* \sqrt{R^* \delta_n} \tag{32}$$

where E^* is the equivalent Young’s modulus and R^* is the equivalent radius which can be written as follows:

$$\frac{1}{R^*} = \frac{1}{R_i} + \frac{1}{R_j} \tag{33}$$

$$\frac{1}{E^*} = \frac{1 - \nu_i^2}{E_{y_i}} + \frac{1 - \nu_j^2}{E_{y_j}} \tag{34}$$

where R_i and R_j are the radius, E_{y_i} and E_{y_j} are Young’s modulus, and ν_i and ν_j are the Poisson’s ratio of each

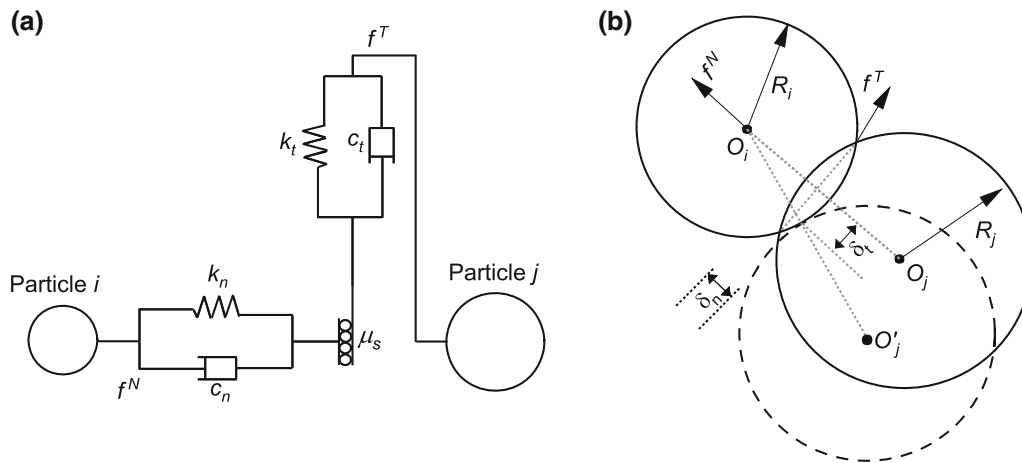


Fig. 15 **a** Rheological scheme and **b** schematic sketch of the Hertz-Mindlin contact model used in this study to simulate fluidisation of soil specimen

neighbouring spheres in contact. The viscoelastic damping constant (c_n) is given by:

$$c_n = -2\sqrt{\frac{5}{6}}\beta\sqrt{S_n m^*} \geq 0 \tag{35}$$

where m^* is the equivalent mass and is given by:

$$\frac{1}{m^*} = \frac{1}{m_i} + \frac{1}{m_j} \tag{36}$$

β and S_n are given by:

$$\beta = \frac{\ln e_r}{\sqrt{\ln^2 e_r + \pi^2}} \tag{37}$$

$$S_n = 2E^* \sqrt{R^* \delta_n} \tag{38}$$

where e_r is the coefficient of restitution. The tangential contact force (f^T) is given by:

$$f^T = k_t \delta_t - c_t v_t^{rel} \tag{39}$$

where k_t is the elastic constant for tangential contact, c_t is the viscoelastic damping constant for tangential contact, δ_t is the tangential overlap, and v_t^{rel} is the tangential component of the relative velocity of two spherical particles, and k_t is given by:

$$k_t = 8G^* \sqrt{R^* \delta_n} \tag{40}$$

with G^* as the equivalent shear modulus, and c_t is written as follows:

$$c_t = -2\sqrt{\frac{5}{6}}\beta\sqrt{k_t m^*} \geq 0 \tag{41}$$

The f^T is limited by:

$$f^T = \mu_s f^N \tag{42}$$

where μ_s is the coefficient of sliding friction.

Acknowledgements The financial support from the Transport Research Centre, University of Technology Sydney, Sydney, Australia, is expressly recognised.

Funding Open Access funding enabled and organized by CAUL and its Member Institutions.

Data availability The data will be made available by the authors upon reasonable request.

Declarations

Conflict of interest The authors state that they are not aware of any competing financial interests or personal relationships that may have influenced the work reported in this paper.

Open Access This article is licensed under a Creative Commons Attribution 4.0 International License, which permits use, sharing, adaptation, distribution and reproduction in any medium or format, as long as you give appropriate credit to the original author(s) and the source, provide a link to the Creative Commons licence, and indicate if changes were made. The images or other third party material in this article are included in the article’s Creative Commons licence, unless indicated otherwise in a credit line to the material. If material is not included in the article’s Creative Commons licence and your intended use is not permitted by statutory regulation or exceeds the permitted use, you will need to obtain permission directly from the copyright holder. To view a copy of this licence, visit <http://creativecommons.org/licenses/by/4.0/>.

References

1. Abbireddy COR, Clayton CRI (2010) Varying initial void ratios for DEM simulations. *Geotechnique* 60:497–502. <https://doi.org/10.1680/geot.2010.60.6.497>
2. Arivalagan J, Rujikiatkamjorn C, Indraratna B, Warwick A (2021) The role of geosynthetics in reducing the fluidisation potential of soft subgrade under cyclic loading. *Geotext Geomembr.* <https://doi.org/10.1016/j.geotexmem.2021.05.004>
3. Barreto D (2009) Numerical and experimental investigation into the behaviour of granular materials under generalised stress states. Ph.D. Thesis, University of London

4. Benseghier Z, Cuéllar P, Luu LH et al (2020) A parallel GPU-based computational framework for the micromechanical analysis of geotechnical and erosion problems. *Comput Geotech* 120:103404
5. Bhatnagar PL, Gross EP, Krook M (1954) A model for collision processes in gases. I. Small amplitude processes in charged and neutral one-component systems. *Phys Rev* 94:511–525. <https://doi.org/10.1103/PhysRev.94.511>
6. Catalano E, Chareyre B, Barthélemy E (2014) Pore-scale modeling of fluid-particle interaction and emerging poromechanical effects. *Int J Numer Anal Methods Geomech* 38:51–71
7. Chawla S, Shahu JT (2016) Reinforcement and mud-pumping benefits of geosynthetics in railway tracks: model tests. *Geotext Geomembr* 44:366–380. <https://doi.org/10.1016/j.geotextmem.2016.01.005>
8. Chen S, Martínez D, Mei R (1996) On boundary conditions in lattice Boltzmann methods. *Phys Fluids* 8:2527–2536. <https://doi.org/10.1063/1.869035>
9. Cundall PA (1988) Computer simulations of dense sphere assemblies. *Stud Appl Mech* 20:113–123. <https://doi.org/10.1016/B978-0-444-70523-5.50021-7>
10. Cundall PA, Drescher A, Strack ODL (1982) Numerical experiments on granular assemblies; measurements and observations. In: *Deform Fail Granul Mater IUTAM Symp Delft* 355–370
11. Cundall PA, Strack ODL (1979) A discrete numerical model for granular assemblies. *Géotechnique* 29:47–65. <https://doi.org/10.1680/geot.1979.29.1.47>
12. Cundall PA, Strack ODL (1983) Modeling of microscopic mechanisms in granular material. *Stud Appl Mech* 7:137–149. <https://doi.org/10.1016/B978-0-444-42192-0.50018-9>
13. Duong TV, Cui YJ, Tang AM et al (2014) Investigating the mud pumping and interlayer creation phenomena in railway substructure. *Eng Geol* 171:45–58. <https://doi.org/10.1016/j.enggeo.2013.12.016>
14. Ergun S (1952) Fluid flow through randomly packed beds. *Chem Eng Prog* 48:89–94
15. Fonseca J, O'Sullivan C, Coop MR, Lee PD (2013) Quantifying the evolution of soil fabric during shearing using scalar parameters. *Geotechnique* 63:818–829. <https://doi.org/10.1680/geot.11.P.150>
16. Fonseca J, O'Sullivan C, Coop MR, Lee PD (2013) Quantifying the evolution of soil fabric during shearing using directional parameters. *Geotechnique* 63:487–499. <https://doi.org/10.1680/geot.12.P.003>
17. Galindo-Torres SA, Scheuermann A, Mühlhaus HB, Williams DJ (2015) A micro-mechanical approach for the study of contact erosion. *Acta Geotech* 10:357–368. <https://doi.org/10.1007/s11440-013-0282-z>
18. Han Y, Cundall P (2017) Verification of two-dimensional LBM-DEM coupling approach and its application in modeling episodic sand production in borehole. *Petroleum* 3:179–189. <https://doi.org/10.1016/j.petlm.2016.07.001>
19. Han K, Feng YT, Owen DRJ (2007) Numerical simulations of irregular particle transport in turbulent flows using coupled LBM-DEM. *C Comput Model Eng Sci* 18:87–100
20. Han K, Feng YT, Owen DRJ (2007) Coupled lattice Boltzmann and discrete element modelling of fluid-particle interaction problems. *Comput Struct* 85:1080–1088. <https://doi.org/10.1016/j.compstruc.2006.11.016>
21. Harshani HMD, Galindo-Torres SA, Scheuermann A, Mühlhaus HB (2015) Micro-mechanical analysis on the onset of erosion in granular materials. *Philos Mag* 95:3146–3166. <https://doi.org/10.1080/14786435.2015.1049237>
22. Hu Z, Zhang Y, Yang Z (2019) Suffusion-induced deformation and microstructural change of granular soils: a coupled CFD-DEM study. *Acta Geotech* 14:795–814. <https://doi.org/10.1007/s11440-019-00789-8>
23. Huang X, Hanley KJ, O'Sullivan C, Kwok FCY (2014) Effect of sample size on the response of DEM samples with a realistic grading. *Particuology* 15:107–115. <https://doi.org/10.1016/j.partic.2013.07.006>
24. Hudson A, Watson G, Le Pen L, Powrie W (2016) Remediation of mud pumping on a ballasted railway track. *Procedia Eng* 143:1043–1050. <https://doi.org/10.1016/j.proeng.2016.06.103>
25. Imole OI, Kumar N, Magnanimo V, Luding S (2012) Hydrostatic and shear behavior of frictionless granular assemblies under different deformation conditions. *KONA Powder Part J* 30:84–108. <https://doi.org/10.14356/kona.2013011>
26. Indraratna B, Haq S, Rujikiatkamjorn C, Israr J (2021) Micro-scale boundaries of internally stable and unstable soils. *Acta Geotech*. <https://doi.org/10.1007/s11440-021-01321-7>
27. Indraratna B, Israr J, Li M (2017) Inception of geohydraulic failures in granular soils—an experimental and theoretical treatment. *Géotechnique* 68:233–248. <https://doi.org/10.1680/jgeot.16.P.227>
28. Indraratna B, Israr J, Rujikiatkamjorn C (2015) Geometrical method for evaluating the internal instability of granular filters based on constriction size distribution. *J Geotech Geoenviron Eng* 141:04015045. [https://doi.org/10.1061/\(ASCE\)GT.1943-5606.0001343](https://doi.org/10.1061/(ASCE)GT.1943-5606.0001343)
29. Indraratna B, Phan NM, Nguyen TT, Huang J (2021) Simulating subgrade fluidization using LBM-DEM coupling. *ASCE Int J Geomech* 21:1–14. [https://doi.org/10.1061/\(ASCE\)GM.1943-5622.0001997](https://doi.org/10.1061/(ASCE)GM.1943-5622.0001997)
30. Indraratna B, Singh M, Nguyen TT et al (2020) Laboratory study on subgrade fluidization under undrained cyclic triaxial loading. *Can Geotech J* 57:1767–1779. <https://doi.org/10.1139/cgj-2019-0350>
31. Jiang MJ, Konrad JM, Leroueil S (2003) An efficient technique for generating homogeneous specimens for DEM studies. *Comput Geotech* 30:579–597. [https://doi.org/10.1016/S0266-352X\(03\)00064-8](https://doi.org/10.1016/S0266-352X(03)00064-8)
32. Kawano K, Shire T, O'Sullivan C (2018) Coupled particle-fluid simulations of the initiation of suffusion. *Soils Found* 58:972–985. <https://doi.org/10.1016/j.sandf.2018.05.008>
33. Kloss C, Goniva C, Hager A et al (2012) Models, algorithms and validation for opensource DEM and CFD-DEM. *Prog Comput Fluid Dyn Int J* 12:140. <https://doi.org/10.1504/PCFD.2012.047457>
34. Latt J (2008) Choice of units in lattice Boltzmann simulations, pp 1–6
35. Li M, Fannin RJ (2012) A theoretical envelope for internal instability of cohesionless soil. *Géotechnique* 62:77–80. <https://doi.org/10.1680/geot.10.T.019>
36. Ma Q, Wautier A, Zhou W (2021) Microscopic mechanism of particle detachment in granular materials subjected to suffusion in anisotropic stress states. *Acta Geotech* 16:2575–2591. <https://doi.org/10.1007/s11440-021-01301-x>
37. Mindlin RD, Deresiewicz H (1989) Elastic spheres in contact under varying oblique forces. In: *The collected papers of Raymond D. Mindlin*, vol I, pp 269–286
38. Nguyen TT, Indraratna B (2020) A coupled CFD-DEM approach to examine the hydraulic critical state of soil under increasing hydraulic gradient. *ASCE Int J Geomech* 20:04020138. [https://doi.org/10.1061/\(ASCE\)gm.1943-5622.0001782](https://doi.org/10.1061/(ASCE)gm.1943-5622.0001782)
39. Nguyen TT, Indraratna B (2020) The energy transformation of internal erosion based on fluid-particle coupling. *Comput Geotech* 121:103475. <https://doi.org/10.1016/j.compgeo.2020.103475>
40. Nguyen TT, Indraratna B, Kelly R et al (2019) Mud pumping under railtracks: mechanisms, assessments and solutions. *Aust Geomech J* 54:59–80

41. Noble DR, Torczynski JR (1998) A Lattice-Boltzmann method for partially saturated computational cells. *Int J Mod Phys C* 09:1189–1201. <https://doi.org/10.1142/S0129183198001084>
42. O'Sullivan C (2011) *Particulate discrete element modelling—a geomechanics perspective*. Spon Press, London
43. Potyondy DO, Cundall PA (2004) A bonded-particle model for rock. *Int J Rock Mech Min Sci* 41:1329–1364. <https://doi.org/10.1016/j.ijrmms.2004.09.011>
44. Rettinger C, Rude U (2017) A comparative study of fluid-particle coupling methods for fully resolved lattice Boltzmann simulations. *Comput Fluids* 154:74–89. <https://doi.org/10.1016/j.compfluid.2017.05.033>
45. Seil P (2016) *LBDEMcoupling: implementation, validation, and applications of a coupled open-source solver for fluid-particle systems*. Ph.D. Thesis, JKU Johannes Kepler Universität Linz
46. Seil P, Pirker S, Lichtenegger T (2018) Onset of sediment transport in mono- and bidisperse beds under turbulent shear flow. *Comput Part Mech* 5:203–212. <https://doi.org/10.1007/s40571-017-0163-6>
47. Senetakis K, Coop MR, Todisco MC (2013) Tangential load-deflection behaviour at the contacts of soil particles. *Geotech Lett* 3:59–66. <https://doi.org/10.1680/geolett.13.00019>
48. Sufian A, Artigaut M, Shire T, O'Sullivan C (2021) Influence of fabric on stress distribution in gap-graded soil. *J Geotech Geoenviron Eng* 147:04021016. [https://doi.org/10.1061/\(ASCE\)GT.1943-5606.0002487](https://doi.org/10.1061/(ASCE)GT.1943-5606.0002487)
49. Ten Cate A, Nieuwstad CH, Derksen JJ, Van den Akker HEA (2002) Particle imaging velocimetry experiments and lattice-Boltzmann simulations on a single sphere settling under gravity. *Phys Fluids* 14:4012–4025. <https://doi.org/10.1063/1.1512918>
50. Thornton C (2000) Numerical simulations of deviatoric shear deformation of granular media. *Geotechnique* 50:43–53
51. Thornton C, Antony SJ (1998) Quasi-static deformation of particulate media. *Philos Trans R Soc A Math Phys Eng Sci* 356:2763–2782. <https://doi.org/10.1098/rsta.1998.0296>
52. Thornton C, Yang F, Seville J (2015) A DEM investigation of transitional behaviour in gas-fluidised beds. *Powder Technol* 270:128–134. <https://doi.org/10.1016/j.powtec.2014.10.017>
53. Tsuji Y, Tanaka T, Ishida T (1992) Lagrangian numerical simulation of plug flow of cohesionless particles in a horizontal pipe. *Powder Technol* 71:239–250. [https://doi.org/10.1016/0032-5910\(92\)88030-L](https://doi.org/10.1016/0032-5910(92)88030-L)
54. Wautier A, Bonelli S, Nicot F (2018) Flow impact on granular force chains and induced instability. *Phys Rev E* 98:42909. <https://doi.org/10.1103/PhysRevE.98.042909>
55. Wu S, Chen Y, Zhu Y et al (2021) Study on filtration process of geotextile with LBM-DEM-DLVO coupling method. *Geotext Geomembr* 49:166–179. <https://doi.org/10.1016/j.geotexmem.2020.09.011>

Publisher's Note Springer Nature remains neutral with regard to jurisdictional claims in published maps and institutional affiliations.